NANO LETTERS

pubs.acs.org/NanoLett Letter

Single-Molecule Fluorescence Lifetime Imaging Using Wide-Field and Confocal-Laser Scanning Microscopy: A Comparative Analysis

Nazar Oleksiievets,[‖] Christeena Mathew,[‖] Jan Christoph Thiele, José Ignacio Gallea, Oleksii Nevskyi, Ingo Gregor, André Weber, Roman Tsukanov,* and Jörg Enderlein*

Cite This: *Nano Lett.* 2022, 22, 6454–6461 Read Online

ACCESS | Metrics & More | Article Recommendations | Supporting Information

ABSTRACT: A recent addition to the toolbox of super-resolution microscopy methods is fluorescence-lifetime single-molecule localization microscopy (FL-SMLM). The synergy of SMLM and fluorescence-lifetime imaging microscopy (FLIM) combines superior image resolution with lifetime information and can be realized using two complementary experimental approaches: confocal-laser scanning microscopy (CLSM) or wide-field microscopy. Here, we systematically and comprehensively compare these two novel FL-SMLM approaches in different spectral regions. For wide-field FL-SMLM, we use a commercial lifetime camera, and for CLSM-based FL-SMLM we employ a home-built system equipped with a rapid scan unit and a single-photon detector. We characterize the performances of the two systems in localizing single emitters in 3D by combining FL-SMLM with metal-induced energy transfer (MIET) for localization along the third dimension and in the lifetime-based multiplexed bioimaging using DNA-PAINT. Finally, we discuss advantages and disadvantages of wide-field and confocal FL-SMLM and provide practical advice on rational FL-SMLM experiment design.

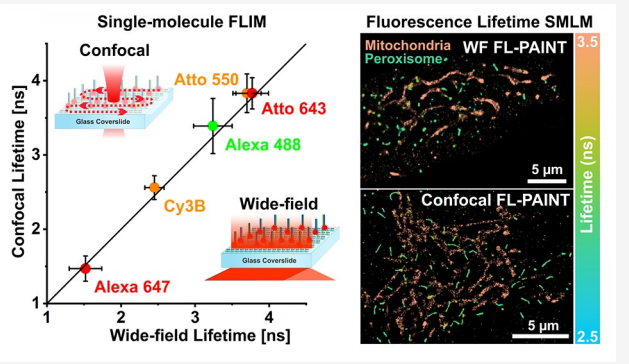

KEYWORDS: *super-resolution microscopy, single-molecule localization microscopy, fluorescence lifetime, DNA-PAINT, fluorescence lifetime imaging microscopy, metal-induced energy transfer*

Super-resolution microscopy has become an indispensable tool in the life sciences. One of its most successful and widely applied variants is single-molecule localization microscopy (SMLM), such as photoactivatable localization microscopy (PALM),[1] stochastic optical reconstruction microscopy (STORM),[2] direct STORM (dSTORM),[3] points accumulation for imaging in nanoscale topography (PAINT),[4] or its more popular variant DNA-PAINT.[5,6] Recently, SMLM was extended to the realm of fluorescence lifetime imaging microscopy (FLIM). Conventional (non-super-resolution) FLIM by itself has found multiple applications across many research fields ranging from material sciences to biology and medicine.[7,8] A particularly attractive FLIM application is lifetime-based multiplexed imaging of cells, where lifetime information combined with spectral separation allows for the simultaneous imaging of different targets inside a cell.[9,10] Recent technical developments allowed for combining FLIM with SMLM to realize fluorescence lifetime SMLM (FL-SMLM).[11−13]

There exist two fundamentally different experimental approaches to realize FL-SMLM: one is based on time-resolved confocal laser-scanning microscopy (CLSM), here CLSM-based FL-SMLM, and the other is based on wide-field microscopy with a time-resolved position sensitive detector, here wide-field FL-SMLM; see Figure 1a. In CLSM-based FLIM, pulsed laser excitation is combined with detection by a single-photon avalanche diode (SPAD) and a high-speed electronics for realizing time-correlated single-photon counting (TCSPC) lifetime measurement at each scan position. When using a (nonresonant) fast scanner, CLSM image acquisition speeds can reach video rates. This allows one to use such a CLSM instrument for SMLM;[12] see Figure 1b. A fundamental advantage of CLSM-based FL-SMLM is the efficient suppression of out-of-focus light and its optical sectioning capability. In addition, CLSM with a nonresonant scanner is very flexible with respect to selecting regions of interest (ROIs), and it does not suffer from pixelation effects as encountered in wide-field SMLM when using pixel array detectors. The main limitation of CLSM-based SMLM is the low photon yield (due to the limited time a molecule is excited and detected during one scan), which limits the overall image

Received: April 20, 2022
Revised: June 14, 2022
Published: July 6, 2022

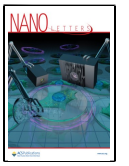

https://doi.org/10.1021/acs.nanolett.2c01586
Nano Lett. 2022, 22, 6454–6461

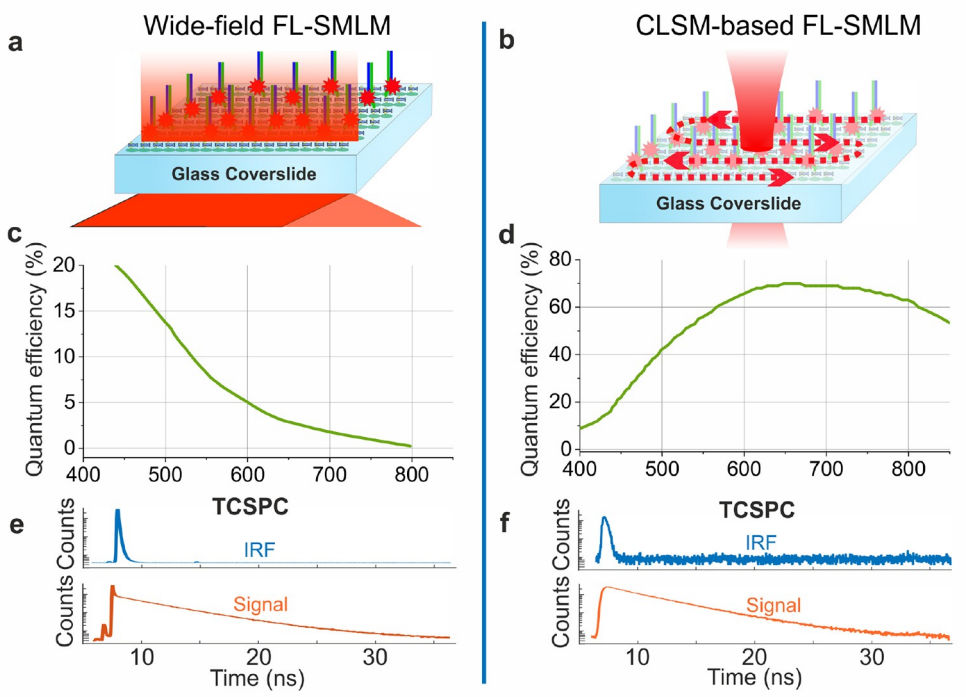

Figure 1. Wide-field and CLSM-based FL-SMLM. (a) Surface-immobilized single fluorophores excited in total internal reflection (TIR) mode. (b) Same sample imaged via CLSM (bidirectional scanning). (c) Quantum efficiency of the lifetime camera LINCam25. (d) Quantum efficiency of the SPAD (single-photon counting module) Excelitas SPCM-AQRH. Data taken from https://photonscore.de and https://www.excelitas.com, respectively. Exemplary TCSPC histograms of the instrument response function (IRF) and signal for wide-field (e) and CLSM-based (f) FL-SMLM.

acquisition speed. This image acquisition speed scales with the area of the ROI, which is typically limited to ca. 20 × 20 μm^2 when using an objective with 100× magnification. In contrast, wide-field FL-SMLM offers fast image acquisition rates. However, for many years, the sensitivity and background of wide-field FLIM made its application to SMLM impossible, although there had been reports of using multichannel plate detectors for single-molecule spectroscopy; see, e.g., ref 14. The recent introduction of the SPAD array has changed the game considerably.[15−17] Interesting alternatives to SPAD arrays are lifetime-measuring cameras,[16,18,19] electro-optical devices,[20] or gated optical image intensifiers.[21] The recently introduced commercial TCSPC camera LINCam25 (Photonscore GmbH, Germany) uses a microchannel plate (MCP)[22] for determining photon arrival times and a charge division anode for positional read-out.[23,24] Despite its relatively low quantum efficiency of photon detection, the camera is capable of imaging single molecules with a reasonable signal-to-noise ratio (SNR) even in the most challenging far-red spectral region, where its quantum efficiency is as low as 2%;[19] see Figure 1c. This is due to the virtually absent detector noise which enables a reasonable SNR even at a very low signal. In comparison, the typical quantum yield of SPAD arrays is better than 50% across the whole visible spectrum (see Figure 1d), but SPAD arrays have much higher dark count rates and they suffer from considerable pixel-to-pixel heterogeneity, low fill factors (which can be partially compensated by suitable microlens arrays), and cross-talk between neighboring pixels.

In the past, we have demonstrated the usefulness of FL-SMLM for multiplexed super-resolution bioimaging[12,13] by utilizing both wide-field and CLSM-based FL-SMLM. However, a thorough comparison of the performance of both methods is missing. Here, we provide a systematic comparison of wide-field and CLSM-based FL-SMLM for fluorophores emitting across the whole visible spectrum and which are widely used in bioimaging. We analyze advantages and disadvantages of wide-field and CLSM-based FL-SMLM, in particular when using FL-SMLM together with metal-induced energy transfer (MIET)[25] for 3D-SMLM, and when employing FL-SMLM for lifetime-multiplexed super-resolution imaging.[12,13]

In order to compare the performances of wide-field and CLSM-based FL-SMLM, we imaged single fluorophores commonly used in single-molecule assays and super-resolution microscopy. The selected fluorophores (Alexa 488, Cy3B/Atto 550 and Alexa 647/Atto 643) emitting in three different spectral regions: green (Alexa 488), orange (Cy3B/Atto 550), and far-red (Alexa 647/Atto 643). The fluorophore-tagged DNA bound to a coverslip surface via biotin-neutravidin, and imaged using the wide-field and CLSM setups; see Figure 1a,b. Detailed schematics of the wide-field and CLSM setups are shown in Figure S1 in the Supporting Information (SI). Using DNA molecules provides flexibility in the surface immobilization of different fluorophores, and it improves their photophysical properties.[19] The quantum efficiency and instrument response function (IRF) of the detectors for both techniques are shown in Figure 1c−f.

FL-SMLM images for the all studied fluorophore types are shown in Figure S2 in the SI. During data analysis, single emitters were localized in the intensity images and then the photons collected from individual localized fluorophores were used to create TCSPC histograms. Fluorescence lifetime values were determined with a maximum likelihood estimator (MLE) monoexponential tail-fit of TCSPC curves, as detailed in the

https://doi.org/10.1021/acs.nanolett.2c01586
Nano Lett. 2022, 22, 6454−6461

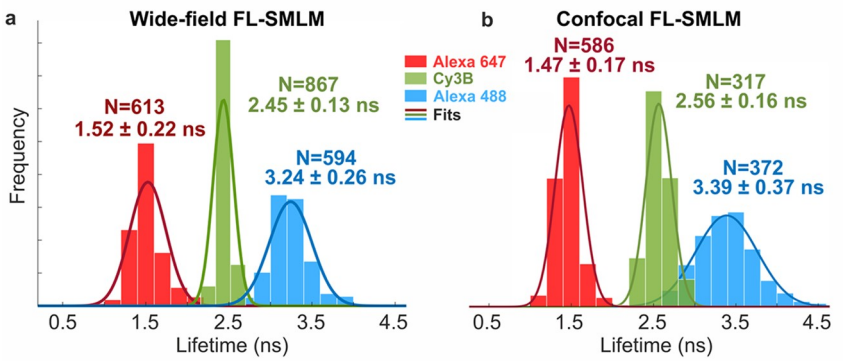

Figure 2. Performance of fluorescence lifetime determination in wide-field and CLSM-based FL-SMLM in different spectral regions. Shown are histograms of lifetime values with corresponding single-Gaussian fits for Alexa 647, Cy3B, and Alexa 488 imaged using the wide-field (a) and the CLS (b) setups. Average lifetime values and standard deviations for each fit are shown next to each peak. *N* is the number of molecules used for each lifetime histogram.

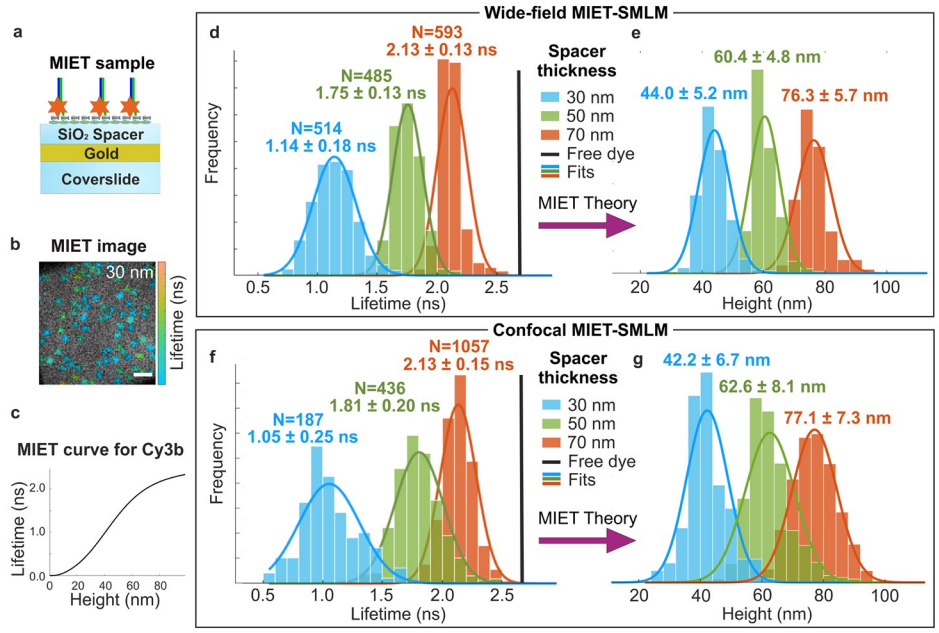

Figure 3. MIET imaging. The dye Cy3B that emits in the orange spectral region was chosen for evaluating and comparing the performances of wide-field and CLSM-based MIET imaging. (a) Sample geometry for MIET experiments. (b) Exemplary MIET image for a sample with 30 nm SiO_2 spacer. (c) Theoretical MIET lifetime-versus-height curve. (d,e) Lifetime and corresponding height histograms of single molecules imaged on top of different SiO_2 spacers with different thickness using wide-field FL-SMLM setup. (f,g) Same as (d) and (e) but when using the CLSM-based FL-SMLM setup. The measured emitter heights include extra distance of 12 nm due to the immobilization layers.

"Wide-field and confocal FL-SMLM Data Analysis" section in the SI. Histograms of the resulting single-molecule lifetime distributions are shown in Figure 2 for the dyes Alexa 488, Cy3B, and Alexa 647, and corresponding histograms for the additional dyes Atto 550 and Atto 643 are shown in Figure S3 in the SI. To reduce the statistical uncertainty, single-molecule data for each fluorophore type that were measured in two to four different ROIs were combined together. The number of molecules used in each lifetime histogram in Figure 2 and the average number of photons emitted before photobleaching are listed in Table S1 in the SI. Finally, histograms of lifetime distributions of each type of fluorophores were fitted with Gaussian distributions, and average values and standard deviations were calculated; see Table S1 in the SI. A comparison of lifetimes between wide-field and confocal FL-SMLM is presented in Figure 2 and in Figure S4 in the SI.

When imaging in the far-red spectral region (Alexa 647), CLSM-based FL-SMLM provided better precision in lifetime determination (1.47 ± 0.17 ns) than wide-field (1.52 ± 0.22 ns); see Figure 2. For the extremely bright Atto 643 dye, we obtained nearly similar precision in lifetime determination for both approaches: 3.77 ± 0.22 ns for wide-field and 3.83 ± 0.21 ns CLSM-based FL-SMLM. In the far-red spectral region, the detection efficiency of the lifetime camera is only ~2%, making the CLSM-based FL-SMLM generally the better choice for imaging. For Cy3B, which emits in the orange spectral region, we obtained fluorescence lifetime values of 2.45 ± 0.13 and 2.56 ± 0.16 ns when using the wide-field and CLSM setups, respectively. And we found roughly similar performances for both systems in that spectral region for Atto 550, with lifetimes values of 3.70 ± 0.19 and 3.83 ± 0.25 ns; see Figure S3 in the SI. For Alexa 488 in the green spectral region, the obtained lifetimes were 3.24 ± 0.26 and 3.39 ± 0.37 ns for the wide-field

https://doi.org/10.1021/acs.nanolett.2c01586
Nano Lett. 2022, 22, 6454−6461

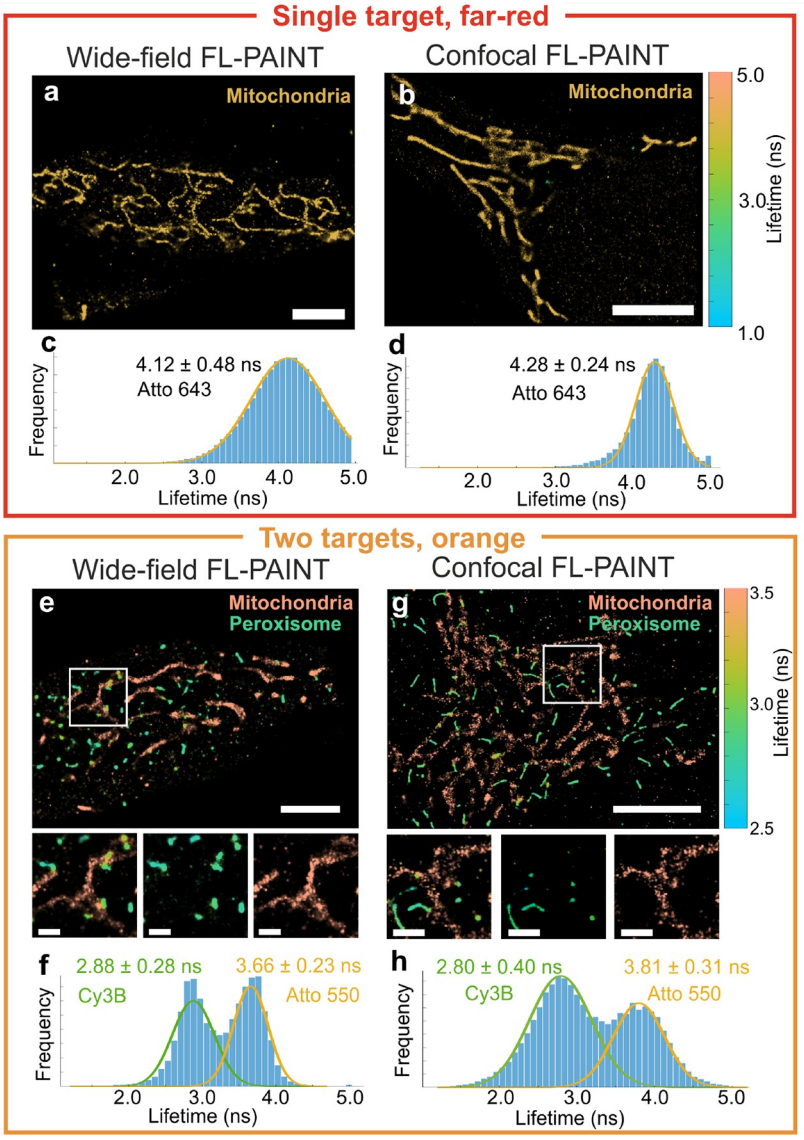

Figure 4. FL-PAINT imaging of fixed HeLa cells. (a–d) Single-target wide-field (a) and confocal (b) FL-PAINT images of mitochondria labeled with the imager P3-Atto 643, and the corresponding lifetime histograms fitted with single-Gaussian distributions (c,d). The average lifetime and standard deviation of each fit are shown. (e-h) Double-target wide-field (e) and confocal (g) FL-PAINT images of mitochondria and peroxisomes labeled with imagers R4-Atto 550 and P3-Cy3B, respectively. Bottom: zoom-in of regions depicted in white rectangles in the cell images (e,g) with separation into two different targets. Zoom-in scale bars are 2 μm. (f,h) The corresponding lifetime histograms fitted with double-Gaussian fits. Lifetime color bars are shown on the right-hand side of the images. Scale bars in (a,b,e,g) are 5 μm.

and CLSM setups, respectively. For the green spectral region, the precision in lifetime determination is better for the lifetime camera. In all cases, the average numbers of detected photons before photobleaching were slightly larger with the lifetime camera than those obtained with the confocal microscope; see detailed list of number of photons emitted for each fluorophore type in Table S1 in the SI. In summary, the precision of lifetime determination is better for wide-field FL-SMLM in the green and orange spectral regions but worse in the far-red, as compared to CLSM-based FL-SMLM.

As the next step, we combined metal-induced energy transfer (MIET)[26−28] with FL-SMLM for three-dimensional single-molecule localization. MIET is based on the electrodynamic coupling of the excited state of a fluorescent emitter to surface plasmons in a thin metal film, which leads to a strongly distance-dependent fluorescence lifetime of the emitter; see Figure 3a–c. Converting the measured fluorescence lifetime into an axial distance allows for axial localization of an emitter with nanometer accuracy.[29] For comparing the performances of wide-field and CLSM-based FL-SMLM for their application in 3D MIET-SMLM, we chose the fluorophore Cy3B emitting in the orange spectral region. Using the dsDNA-biotin-neutravidin surface immobilization strategy, as detailed in the SI, single Cy3B molecules were immobilized on top of a substrate consisting of a coverslip covered with a thin gold film (10 nm) for MIET and with an additional SiO_2 spacer of well-known thickness that allowed us to keep fluorescent molecules at well-defined distances from the metal layer; see Figure 3a for sample geometry. We prepared three different substrates with 30, 50, and 70 nm thick layers of SiO_2, respectively. The presence of the biotin-neutravidin immobilization layers added an extra height of ∼12 nm to the distance between fluorophores and metal layer.[30] Thus, the design values of the distances between fluorophores and the gold layer were 42,

https://doi.org/10.1021/acs.nanolett.2c01586
Nano Lett. 2022, 22, 6454−6461

62, and 82 nm. Conversion of experimentally measured lifetime values to distance values was done using a theoretical MIET model; see ref 26. The calculated MIET curve for Cy3B is shown in Figure 3c. Imaging was done by using both the wide-field and the CLSM-based setups. We assessed the performances of both techniques based on the lifetime histograms and corresponding height histograms; see Figure 3d,e for wide-field MIET-SMLM and Figure 3f,g for CLSM-based MIET-SMLM. MIET-SMLM images of single Cy3B fluorophores immobilized on top of SiO_2 spacers with different thicknesses are shown in Figure S5 in the SI.

First, we note the remarkable agreement between the average lifetime and corresponding height values obtained with both the wide-field and the confocal setups; see Figure 3d−g. We list theoretical and measured lifetime values in Table S2 as well as corresponding height values in Table S3 in the SI. The number of analyzed molecules and the average numbers of detected photons per molecule for each spacer thickness are given in Table S4 in the SI. For a direct comparison, we plotted the lifetime and height values for both wide-field and confocal measurements in Figure S6 in the SI. For all spacers, there is excellent agreement between the design and experimentally measured values. The precision of lifetime (and subsequently height) determination is slightly better for wide-field MIET-SMLM, due to its improved sensitivity in the orange spectral region. Average lateral localization precision values for all MIET-SMLM images were calculated using a modified Mortensen equation,[31,32] and they were found to be 18.5 and 11.5 nm for the wide-field and CLSM-based measurements, respectively, as listed in detail in Table S5 in the SI.

In this part, we present FL-SMLM images of HeLa cells obtained with DNA-PAINT and we compare the performances of wide-field and CLSM-based FL-SMLM for multitarget bioimaging. The key advantage of DNA-PAINT is that it is unaffected by photobleaching due to the continuous exchange of fluorophores during image acquisition. In addition, due to the orthogonality of DNA hybridization, multiple targets can be independently addressed by using different DNA sequences. Moreover, using fluorophores that emit in the same spectral region for labeling different targets avoids any chromatic aberration artifacts. Recently, it has been shown that the fluorescence lifetime can be used for multiplexing in multi-target DNA-PAINT imaging of cells (FL-PAINT).[13] In FL-PAINT, one uses fluorophores that differ only in their lifetime values but are very similar in their emission spectra. FL-PAINT allows for simultaneous imaging of different targets, in contrast to the need of sequential imaging in commonly used Exchange-PAINT,[33,34] which speeds up multitarget image acquisition.

Both wide-field and confocal FL-PAINT imaging in the orange spectral region have been demonstrated before;[13] however, no comprehensive comparison of both methods has been done. To do this, we performed single- and double-target FL-PAINT imaging of peroxisomes and mitochondria in fixed HeLa cells both in the far-red and orange spectral regions; see Figure 4. Specifically, peroxisomes (PTS1) and mitochondria (TOMM20) were genetically encoded with GFP and BFP, correspondingly, and then labeled with DNA docking strands R4*[35] (or P1*) and P3* via single-domain antibodies (nanobodies), which decreased the distance between target and imager dye.[34] The following pairs of fluorophores were used for double-target imaging: Cy3B and Atto 550 in the orange and Alexa 647 and Atto 643 in the far-red spectral regions. Custom-written Matlab routines were used for the analysis of both wide-field and confocal FL-PAINT data, as detailed in the "FL-PAINT data acquisition and analysis" section in the SI. We found that wide-field FL-PAINT imaging with the lifetime camera LINCam25 is even possible in the most challenging far-red spectral region, but the achievable localization precision is significantly lower than that obtained with confocal FL-PAINT (34 and 10 nm, correspondingly). Further image resolution analysis was done using Fourier Ring Correlation (FRC),[36] and the average resolution of wide-field FL-PAINT and confocal FL-PAINT images in far-red spectral region are 129.7 and 77.5 nm correspondingly. The resulting FRC maps are shown in Figure S7 in the SI.

The image quality of double-target imaging with wide-field FL-PAINT in the far-red spectral region was insufficient to confidently distinguish between the two imaged targets. Therefore, we chose the orange spectral region for double-target wide-field and confocal FL-PAINT imaging; see Figure 4e,g. To identify each target, FL-PAINT data was used to create lifetime histograms, as shown in Figure 4f,h. In both cases, the lifetime histograms had two separate peaks, making lifetime-based target identification straightforward. The calculated crosstalk between the targets for the wide-field and confocal FL-PAINT images is 1.3% and 3.1%, respectively; see Figure S10 in the SI. The average localization precision of the two targets in orange spectral region is 18.5 nm for wide-field and 11.9 nm for confocal FL-PAINT, and the average resolution of wide-field and confocal FL-PAINT images is 69.9 and 61.3 nm, correspondingly. We note that the average lifetime values measured with both techniques are in excellent agreement. Double-target FL-PAINT imaging in the far-red spectral region with the confocal setup is shown in Figure S8 in the SI.

It should be noted that both wide-field and confocal FL-PAINT accumulated localization events with similar rates, as shown in surface-PAINT experiments (described in detail in the SI), where docking strands were attached directly to the surface and localization events were counted for each frame of the recorded movie, see Figure S9a,b in the SI. We also compared the temporal evolution of the visibility of cell features in wide-field and confocal FL-PAINT images by recording images of cells after 5, 15, 30, and 45 min observation time; see Figure S9c,d in the SI. Again, localization events accumulated at similar rates.

In summary, while FL-PAINT works well with both wide-field and confocal setups in the orange spectral region, the wide-field setup is clearly inferior in performance in the far-red spectral region. This is due to the rapid drop of its quantum efficiency of detection toward longer wavelengths. However, in the orange spectral region, where the wide-field setup compares well with the confocal setup, it offers a much better field of view (more then $30 \times 30\ \mu m^2$) than the confocal setup, at same image acquisition speed. In contrast, confocal FL-PAINT offers better out-of-focus light rejection and optical sectioning, which is important when imaging thicker samples.[13] But whatever approach is used, FL-PAINT is a versatile technique that is capable of high-throughput multiplexed imaging and can be readily combined with other multiplexing techniques, for example, Exchange-PAINT,[33] kinetic barcoding via blinking kinetics engineering,[37] or spectral splitting.[38]

The quantitative estimation of the advantages and disadvantages of wide-field and confocal FL-SMLM is important for choosing the best method for a given sample

https://doi.org/10.1021/acs.nanolett.2c01586
Nano Lett. 2022, 22, 6454−6461

to be imaged. In the present paper, we conducted a thorough comparison of both methods using a home-built CLSM instrument equipped with a rapid scan unit and a wide-field setup equipped with a new commercially available TCSPC lifetime camera. One of the surprising results of our comparison is that the wide-field system, despite its low quantum efficiency of detection (below 10%), competes well with the confocal system in the blue-green and orange spectral regions. Only in the far-red spectral region, where its quantum efficiency drops to 2%, the confocal setup becomes clearly better-performing, especially for bioimaging applications, due to its higher quantum efficiency.

The TCSPC camera features extremely low noise but relatively low quantum efficiency, while the single photon counting detector has relatively high quantum efficiency but considerably larger noise. The devices are also very different by the maximal count rates they can register. The LINCam acquisition count rate is limited to ∼1 Mc/s, with an optimum of ∼300 kc/s for time-correlated single photon counting,[13] while SPADs can tolerate acquisition count rates up to ca. ten Mc/s. All these parameters have to be taken into account when choosing the most suitable technique for a particular application. Both the TCSPC camera as well as the SPAD allow for determining fluorescence lifetimes with high accuracy. The TCSPC camera is advantageous for imaging large fields of view where it offers fast acquisition times. In contrast, CLSM-based FL-SMLM is advantageous when one is interested in imaging smaller regions of interest, but with high localization precision, and it is mandatory when imaging in the far-red spectral region.

One of the highly promising applications of FL-SMLM is its combination with MIET for isotropic 3D-SMLM. To demonstrate this, we imaged and localized in 3D single Cy3B fluorophores positioned at well-defined distances above a thin gold layer. Previously, we performed similar experiment with Atto 655 fluorophore using wide-field single-molecule MIET[19] and with Alexa 647 using confocal single-molecule MIET.[29] Here, we compare both methods and find for both methods excellent agreement between the design and determined axial positions. Further improvement of axial resolution to subnanometer scale is possible when replacing the metal by a single sheet of graphene (graphene-induced energy transfer aka GIET; see refs 39, 40) However, the axial distance range over which GIET works is even smaller than that for MIET, restricted to ∼25 nm. Nonetheless, the combination of FL-PAINT with GIET could offer exceptional lateral and axial localization precision which promises to deliver isotropic 3D super-resolution on a molecular nanometer length scale.

■ ASSOCIATED CONTENT

Supporting Information

The Supporting Information is available free of charge at https://pubs.acs.org/doi/10.1021/acs.nanolett.2c01586.

Wide-field and confocal FLIM optical setups, FL-SMLM/MIET-SMLM imaging, FL-SMLM images of single surface-immobilized molecules, comparison of fluorescence lifetimes of wide-field and confocal FL-SMLM, MIET-SMLM imaging of surface-immobilized Cy3B fluorophores, FL-PAINT imaging (PDF)

■ AUTHOR INFORMATION

Corresponding Authors

Roman Tsukanov − *III. Institute of Physics − Biophysics, Georg August University, 37077 Göttingen, Germany;* orcid.org/0000-0002-3967-1755; Phone: +49 551 39 26911; Email: rtsukan@gwdg.de

Jörg Enderlein − *III. Institute of Physics − Biophysics and Cluster of Excellence "Multiscale Bioimaging: from Molecular Machines to Networks of Excitable Cells" (MBExC), Georg August University, 37077 Göttingen, Germany;* orcid.org/0000-0001-5091-7157; Phone: +49 551 39 26908; Email: jenderl@gwdg.de

Authors

Nazar Oleksiievets − *III. Institute of Physics − Biophysics, Georg August University, 37077 Göttingen, Germany*

Christeena Mathew − *Laboratory of Supramolecular Chemistry, EPFL SB ISIC LCS, BCH 3307, CH-1015 Lausanne, Switzerland*

Jan Christoph Thiele − *III. Institute of Physics − Biophysics, Georg August University, 37077 Göttingen, Germany;* orcid.org/0000-0002-6638-6298

José Ignacio Gallea − *III. Institute of Physics − Biophysics, Georg August University, 37077 Göttingen, Germany*

Oleksii Nevskyi − *III. Institute of Physics − Biophysics, Georg August University, 37077 Göttingen, Germany;* orcid.org/0000-0003-2893-481X

Ingo Gregor − *III. Institute of Physics − Biophysics, Georg August University, 37077 Göttingen, Germany;* orcid.org/0000-0002-1775-2159

André Weber − *Combinatorial NeuroImaging Core Facility, Leibniz Institute for Neurobiology, 39118 Magdeburg, Germany;* orcid.org/0000-0001-7752-2112

Complete contact information is available at: https://pubs.acs.org/10.1021/acs.nanolett.2c01586

Author Contributions

‖N.O. and C.M. contributed equally to this work.

Funding

J.E. acknowledges financial support by the DFG through Germany's Excellence Strategy EXC 2067/1-390729940. J.E., N.O., J.C.T., and O.N. are grateful to the European Research Council (ERC) via project "smMIET" (Grant Agreement No. 884488) under the European Union's Horizon 2020 research and innovation program. J.I.G. is grateful to the Deutsche Forschungsgemeinschaft (DFG, German Research Foundation) for financial support via the project A06 of SFB 860. A.W. acknowledges financial support by the Federal Ministry of Education and Research (BMBF TIRAMISU grant number 13N15790) and the Deutsche Forschungsgemeinschaft (DFG SFB 854 TPZ). C.M. acknowledges the CSC Graduate School funded by the French National Research Agency (CSC-IGS ANR-17-EURE-0016) for a M.Sc. fellowship and Erasmus+ Stage.

Notes

The authors declare the following competing financial interest(s): André Weber is part-time employee of Photonscore GmbH. All other authors declare no competing financial interests.

https://doi.org/10.1021/acs.nanolett.2c01586
Nano Lett. 2022, 22, 6454−6461

■ ACKNOWLEDGMENTS

The authors are grateful to Photonscore GmbH and personally to Dr. Yury Prokazov for the initial loan of the LINCam25 system and valuable advise on many occasions. We are grateful to Sven Thoms and Yelena Sargsyan for providing the HeLa cell line, GFP-PTS1 (PST990), and mito-BFP (Addgene plasmid Nr. 49151) and for helping with establishing cell culture in our lab. We are grateful to Anna Chizhik for preparing gold- and SiO_2-covered coverslips and for her help with the cell culture. We thank Felipe Opazo and Nikolaos Mougios for their optimization of cellular target labeling. We thank Alexey Chizhik and Niels Radmacher for the advice.

■ REFERENCES

(1) Betzig, E.; Patterson, G. H.; Sougrat, R.; Lindwasser, O. W.; Olenych, S.; Bonifacino, J. S.; Davidson, M. W.; Lippincott-Schwartz, J.; Hess, H. F. Imaging intracellular fluorescent proteins at nanometer resolution. *Science* **2006**, *313*, 1642−1645.

(2) Rust, M. J.; Bates, M.; Zhuang, X. Sub-diffraction-limit imaging by stochastic optical reconstruction microscopy (STORM). *Nat. Methods* **2006**, *3*, 793.

(3) van de Linde, S.; Loschberger, A.; Klein, T.; Heidbreder, M.; Wolter, S.; Heilemann, M.; Sauer, M. Direct stochastic optical reconstruction microscopy with standard fluorescent probes. *Nat Protoc.* **2011**, *6*, 991−1009.

(4) Sharonov, A.; Hochstrasser, R. M. Wide-field subdiffraction imaging by accumulated binding of diffusing probes. *Proc. Natl. Acad. Sci. U. S. A.* **2006**, *103*, 18911−18916.

(5) Jungmann, R.; Steinhauer, C.; Scheible, M.; Kuzyk, A.; Tinnefeld, P.; Simmel, F. C. Single-molecule kinetics and super-resolution microscopy by fluorescence imaging of transient binding on DNA origami. *Nano Lett.* **2010**, *10*, 4756−4761.

(6) Schnitzbauer, J.; Strauss, M. T.; Schlichthaerle, T.; Schueder, F.; Jungmann, R. Super-resolution microscopy with DNA-PAINT. *Nat. Protoc.* **2017**, *12*, 1198−1228.

(7) Berezin, M. Y.; Achilefu, S. Fluorescence Lifetime Measurements and Biological Imaging. *Chem. Rev.* **2010**, *110*, 2641−2684.

(8) Datta, R.; Heaster, T. M.; Sharick, J. T.; Gillette, A. A.; Skala, M. C. Fluorescence Lifetime Imaging Microscopy: Fundamentals and Advances in Instrumentation, Analysis, and Applications. *J. Biomed. Opt.* **2020**, *25*, 071203.

(9) Niehörster, T.; Löschberger, A.; Gregor, I.; Krämer, B.; Rahn, H.-J.; Patting, M.; Koberling, F.; Enderlein, J.; Sauer, M. Multi-target spectrally resolved fluorescence lifetime imaging microscopy. *Nat. Methods* **2016**, *13*, 257−262.

(10) Frei, M. S.; Tarnawski, M.; Roberti, M. J.; Koch, B.; Hiblot, J.; Johnsson, K. Engineered HaloTag Variants for Fluorescence Lifetime Multiplexing. *Nat. Methods* **2022**, *19*, 65.

(11) Koenderink, A. F.; Tsukanov, R.; Enderlein, J.; Izeddin, I.; Krachmalnicoff, V. Super-resolution imaging: when biophysics meets nanophotonics. *Nanophotonics* **2022**, *11*, 169−202.

(12) Thiele, J. C.; Helmerich, D. A.; Oleksiievets, N.; Tsukanov, R.; Butkevich, E.; Sauer, M.; Nevskyi, O.; Enderlein, J. Confocal Fluorescence-Lifetime Single-Molecule Localization Microscopy. *ACS Nano* **2020**, *14*, 14190−14200.

(13) Oleksiievets, N.; Sargsyan, Y.; Thiele, J. C.; Mougios, N.; Sograte-Idrissi, S.; Nevskyi, O.; Gregor, I.; Opazo, F.; Thoms, S.; Enderlein, J.; Tsukanov, R. Fluorescence lifetime DNA-PAINT for multiplexed super-resolution imaging of cells. *Commun. Biol.* **2022**, *5*, 38.

(14) Brooks Shera, E.; Seitzinger, N. K.; Davis, L. M.; Keller, R. A.; Soper, S. A. Detection of Single Fluorescent Molecules. *Chem. Phys. Lett.* **1990**, *174*, 553−557.

(15) Bruschini, C.; Homulle, H.; Antolovic, I. M.; Burri, S.; Charbon, E. Single-Photon Avalanche Diode Imagers in Biophotonics: Review and Outlook. *Light Sci. Appl.* **2019**, *8*, 87.

(16) Hirvonen, L. M.; Suhling, K. Wide-Field TCSPC: Methods and Applications. *Measurement Science and Technology* **2017**, *28*, 012003.

(17) Ulku, A.; Ardelean, A.; Antolovic, M.; Weiss, S.; Charbon, E.; Bruschini, C.; Michalet, X. Wide-Field Time-Gated SPAD Imager for Phasor-Based FLIM Applications. *Methods and Applications in Fluorescence* **2020**, *8*, 024002.

(18) Suhling, K.; Hirvonen, L. M.; Becker, W.; Smietana, S.; Netz, H.; Milnes, J.; Conneely, T.; Marois, A. L.; Jagutzki, O.; Festy, F.; et al. Wide-Field Time-Correlated Single Photon Counting-Based Fluorescence Lifetime Imaging Microscopy. *Nuclear Instruments and Methods in Physics Research Section A: Accelerators, Spectrometers, Detectors and Associated Equipment* **2019**, *942*, 162365.

(19) Oleksiievets, N.; Thiele, J. C.; Weber, A.; Gregor, I.; Nevskyi, O.; Isbaner, S.; Tsukanov, R.; Enderlein, J. Wide-Field Fluorescence Lifetime Imaging of Single Molecules. *J. Phys. Chem. A* **2020**, *124*, 3494−3500.

(20) Bowman, A. J.; Klopfer, B. B.; Juffmann, T.; Kasevich, M. A. Electro-Optic Imaging Enables Efficient Wide-Field Fluorescence Lifetime Microscopy. *Nat. Commun.* **2019**, *10*, 4561.

(21) Sparks, H.; Görlitz, F.; Kelly, D. J.; Warren, S. C.; Kellett, P. A.; Garcia, E.; Dymoke-Bradshaw, A. K. L.; Hares, J. D.; Neil, M. A. A.; Dunsby, C.; et al. Characterisation of new gated optical image intensifiers for fluorescence lifetime imaging. *Rev. Sci. Instrum.* **2017**, *88*, 013707.

(22) Lampton, M.; Malina, R. F. Quadrant Anode Image Sensor. *Rev. Sci. Instrum.* **1976**, *47*, 1360−1362.

(23) Prokazov, Y.; Turbin, E.; Weber, A.; Hartig, R.; Zuschratter, W. Position sensitive detector for fluorescence lifetime imaging. *Journal of Instrumentation* **2014**, *9*, C12015.

(24) Engelborghs, Y.; Visser, A. J. W. G.; Hartig, R.; Prokazov, Y.; Turbin, E.; Zuschratter, W. *Fluorescence spectroscopy and microscopy*; Humana Press, 2014; Vol. *1076*; pp457−480.

(25) Gregor, I.; Chizhik, A.; Karedla, N.; Enderlein, J. Metal-induced energy transfer. *Nanophotonics* **2019**, *8*, 1689−1699.

(26) Enderlein, J. Single-molecule fluorescence near a metal layer. *Chem. Phys.* **1999**, *247*, 1−9.

(27) Chizhik, A. I.; Rother, J.; Gregor, I.; Janshoff, A.; Enderlein, J. Metal-induced energy transfer for live cell nanoscopy. *Nat. Photonics* **2014**, *8*, 124.

(28) Karedla, N.; Chizhik, A. I.; Gregor, I.; Chizhik, A. M.; Schulz, O.; Enderlein, J. Single-Molecule Metal-Induced Energy Transfer (smMIET): Resolving Nanometer Distances at the Single-Molecule Level. *ChemPhysChem* **2014**, *15*, 705−711.

(29) Thiele, J. C.; Jungblut, M.; Helmerich, D. A.; Tsukanov, R.; Chizhik, A.; Chizhik, A. I.; Schnermann, M. J.; Sauer, M.; Nevskyi, O.; Enderlein, J. Isotropic Three-Dimensional Dual-Color Super-Resolution Microscopy with Metal-Induced Energy Transfer. *Science Advances* **2022**, *8*, 2506.

(30) Isbaner, S.; Karedla, N.; Kaminska, I.; Ruhlandt, D.; Raab, M.; Bohlen, J.; Chizhik, A.; Gregor, I.; Tinnefeld, P.; Enderlein, J.; et al. Axial colocalization of single molecules with nanometer accuracy using metal-induced energy transfer. *Nano Lett.* **2018**, *18*, 2616−2622.

(31) Mortensen, K. I.; Churchman, L. S.; Spudich, J. A.; Flyvbjerg, H. Optimized localization analysis for single-molecule tracking and super-resolution microscopy. *Nat. Methods* **2010**, *7*, 377−381.

(32) Rieger, B.; Stallinga, S. The lateral and axial localization uncertainty in super-resolution light microscopy. *ChemPhysChem* **2014**, *15*, 664−670.

(33) Jungmann, R.; Avendano, M. S; Woehrstein, J. B; Dai, M.; Shih, W. M; Yin, P. Multiplexed 3D cellular super-resolution imaging with DNA-PAINT and Exchange-PAINT. *Nat. Methods* **2014**, *11*, 313−318.

(34) Sograte-Idrissi, S.; Oleksiievets, N.; Isbaner, S.; Eggert-Martinez, M.; Enderlein, J.; Tsukanov, R.; Opazo, F. Nanobody detection of standard fluorescent proteins enables multi-target DNA-PAINT with high resolution and minimal displacement errors. *Cells* **2019**, *8*, 48.

https://doi.org/10.1021/acs.nanolett.2c01586
Nano Lett. 2022, 22, 6454−6461

(35) Strauss, S.; Jungmann, R. Up to 100-fold speed-up and multiplexing in optimized DNA-PAINT. *Nat. Methods* **2020**, *17*, 789−791.
(36) Culley, S.; Albrecht, D.; Jacobs, C.; Pereira, P. M.; Leterrier, C.; Mercer, J.; Henriques, R. Jason andHenriques Quantitative mapping and minimization of super-resolution optical imaging artifacts. *Nat. Methods* **2018**, *15*, 263−266.
(37) Wade, O. K.; Woehrstein, J. B.; Nickels, P. C.; Strauss, S.; Stehr, F.; Stein, J.; Schueder, F.; Strauss, M. T.; Ganji, M.; Schnitzbauer, J.; et al. 124-Color Super-resolution Imaging by Engineering DNA-PAINT Blinking Kinetics. *Nano Lett.* **2019**, *19*, 2641−2646.
(38) Gimber, N.; Strauss, S.; Jungmann, R.; Schmoranzer, J. Simultaneous Multicolor DNA-PAINT without Sequential Fluid Exchange Using Spectral Demixing. *Nano Lett.* **2022**, *22*, 2682−2690.
(39) Ghosh, A.; Sharma, A.; Chizhik, A. I.; Isbaner, S.; Ruhlandt, D.; Tsukanov, R.; Gregor, I.; Karedla, N.; Enderlein, J. Graphene-based metal-induced energy transfer for sub-nanometre optical localization. *Nat. Photonics* **2019**, *13*, 860−865.
(40) Kaminska, I.; Bohlen, J.; Rocchetti, S.; Selbach, F.; Acuna, G. P.; Tinnefeld, P. Distance Dependence of Single-Molecule Energy Transfer to Graphene Measured with DNA Origami Nanopositioners. *Nano Lett.* **2019**, *19*, 4257−4262.

https://doi.org/10.1021/acs.nanolett.2c01586
Nano Lett. 2022, 22, 6454−6461